Magnetoelectric Behavior from $S = 1/2$ Asymmetric Square Cupolas

Yasuyuki Kato,[1] Kenta Kimura,[2] Atsushi Miyake,[3] Masashi Tokunaga,[3] Akira Matsuo,[3] Koichi Kindo,[3]
Mitsuru Akaki,[4] Masayuki Hagiwara,[4] Masakazu Sera,[2] Tsuyoshi Kimura,[2] and Yukitoshi Motome[1]

[1]*Department of Applied Physics, The University of Tokyo, Hongo, 7-3-1, Bunkyo, Tokyo 113-8656, Japan*
[2]*Division of Materials Physics, Graduate School of Engineering Science, Osaka University,
Toyonaka, Osaka 560-8531, Japan*
[3]*Institute for Solid State Physics, The University of Tokyo, Kashiwa, Chiba 277-8581, Japan*
[4]*Center for Advanced High Magnetic Field Science, Graduate School of Science, Osaka University,
Toyonaka, Osaka 560-0043, Japan*
(Received 31 October 2016; revised manuscript received 25 December 2016; published 9 March 2017)

Magnetoelectric properties are studied by a combined experimental and theoretical study of a quasi-two-dimensional material composed of square cupolas, $Ba(TiO)Cu_4(PO_4)_4$. The magnetization is measured up to the field above the saturation, and several anomalies are observed depending on the field directions. We propose a $S = 1/2$ spin model with Dzyaloshinskii-Moriya interactions, which reproduces the full magnetization curves well. Elaborating the phase diagram of the model, we show that the anomalies are explained by magnetoelectric phase transitions. Our theory also accounts for the scaling of the dielectric anomaly observed in the experiments. The results elucidate the crucial role of the in-plane component of Dzyaloshinskii-Moriya interactions, which is induced by the noncoplanar buckling of a square cupola. We also predict a "hidden" phase and another magnetoelectric response, both of which appear in a nonzero magnetic field.

Spatial asymmetry is a source of interesting phenomena in a broad range of condensed matter physics. A well-known example is the molecular asymmetry of water, H_2O, which leads to an electric polarization in each molecule. The asymmetry is also at play in magnets: the loss of inversion symmetry activates the asymmetric interactions through the relativistic spin-orbit coupling, such as the Dzyaloshinskii-Moriya (DM) interaction [1,2]. The asymmetric interactions lead to intriguing magnetism, e.g., weak ferromagnetism in antiferromagnets and spin-spiral ordering in helimagnets. They have also attracted growing interest as an origin of the magnetoelectric (ME) effect, that is, cross-correlations between dielectricity and magnetism [3,4].

Recently, an interesting series of chiral antiferromagnets, $A(TiO)Cu_4(PO_4)_4$ ($A =$ Ba, Sr) with space group $P42_12$, was newly synthesized [5]. The materials have a quasi-two-dimensional structure, composed of an alternating array of Cu_4O_{12} clusters, as shown in Fig. 1(a). Each Cu_4O_{12} cluster consists of four corner-sharing CuO_4 plaquettes, forming a noncoplanar buckled structure termed an (irregular) square cupola. The asymmetric unit can carry ME-active magnetic multipoles [6] associated with Cu spins. Indeed, a divergent anomaly of the dielectric constant was observed at the Néel temperature ($T_N = 9.5$ K) in magnetic fields applied along the [100] and [1$\bar{1}$0] directions for $A =$ Ba [7]. Although the ME response was argued by the magnetic quadrupole associated with noncoplanar antiferromagnetic ordering, the microscopic understanding is not fully obtained. It is highly desirable to clarify how the unique asymmetry

arising from the square cupolas affects the magnetic and dielectric properties in this series of compounds.

In this Letter, combining experimental and theoretical studies, we clarify the microscopic mechanism of ME behavior in $A(TiO)Cu_4(PO_4)_4$. First, from the magnetization measurement for the compound with $A =$ Ba up to the field above the saturation, we find several anomalies depending on the field direction. Then, considering the structural asymmetry, we construct a minimal theoretical
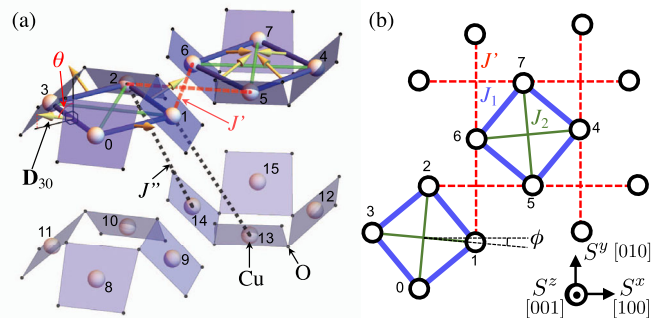

FIG. 1. (a) Schematic of the lattice structure, which includes a pair of upward and downward square cupolas. The spheres and black dots represent Cu cations and O ions, respectively. The yellow arrows on the blue bonds represent the DM vectors $\mathbf{D}_{ij}$ in the model in Eq. (1). The intercupola couplings J' and J'' are also shown. (b) Top view. The blue, green, and red dashed lines represent J_1, J_2, and J' bonds in Eq. (1), respectively.

model, which successfully reproduces the full magnetization curves within a cluster mean field (CMF) approximation. Elaborating the ground-state and finite-temperature (T) phase diagrams of the model, we show that the anomalies originate from ME phase transitions where the in-plane component of the DM vector plays a key role. Furthermore, we successfully reproduce the dielectric anomaly and its scaling behavior observed in the prior experiments [7]. Our results indicate that the series of compounds provides a unique playground where the electric polarization is controllable not only by a magnetic field or T but also by the asymmetry of square cupolas that modulate the orientation of the DM vectors.

Single crystals of $Ba(TiO)Cu_4(PO_4)_4$ were grown by the flux method as described previously [5]. Powder x-ray diffraction (XRD) measurements on crushed single crystals confirmed a single phase. For magnetization measurements, the crystals were oriented using Laue XRD. High-field magnetization, in magnetic fields up to 69 T, was measured at 1.4 K using an induction method with a multilayer pulsed magnet installed at the International MegaGauss Science Laboratory of the Institute for Solid State Physics at The University of Tokyo. Multifrequency electron spin resonance (ESR) measurements (600–1400 GHz) in pulsed magnetic fields were performed to obtain the g values for the field directions along [100], [110], and [001]. The g values were found to be isotropic within the experimental accuracy: $g \sim 2.20(5)$ for the three directions.

Figure 2(a) shows the experimental results of full magnetization curves at $T = 1.4$ K $< T_N$ for the magnetic field (**B**) applied along the [100], [110], and [001] directions. In the low-field region ($B = |\mathbf{B}| < 12$ T), the slope of the magnetization M is smaller for the out-of-plane field (**B**∥[001]) than for in-plane fields (**B**∥[100] and [110]), which is consistent with the previous report [7]. On increasing B, we find a jumplike anomaly in M for all of the B directions, whose critical field is $\sim$12, 19, and 20 T for **B**∥[001], [100], and [110], respectively; the anomalies are more clearly seen in the field derivative dM/dB in Fig. 2(b). On further increasing B above $B \sim 60$ T, the magnetization for all of the B directions shows a saturation at $\sim$1.1μ_B/Cu^{2+}. The saturation-magnetization values are corrected by the g values determined by the ESR. We note that dM/dB shows a hump at $B \sim 40$ T only for **B**∥[001] as shown in Fig. 2(b).

For understanding the peculiar magnetization curves, we consider a localized spin model associated with $S = 1/2$ spin degrees of freedom of each Cu cation. We take into account four dominant exchange interactions [7]: the intracupola exchange interactions J_1 and J_2, together with the two intercupola couplings, intralayer J' and interlayer J'' (see Fig. 1). Besides considering the loss of inversion symmetry at the centers of J_1 bonds, we take into account the DM interaction originating from the spin-orbit coupling. The Hamiltonian reads
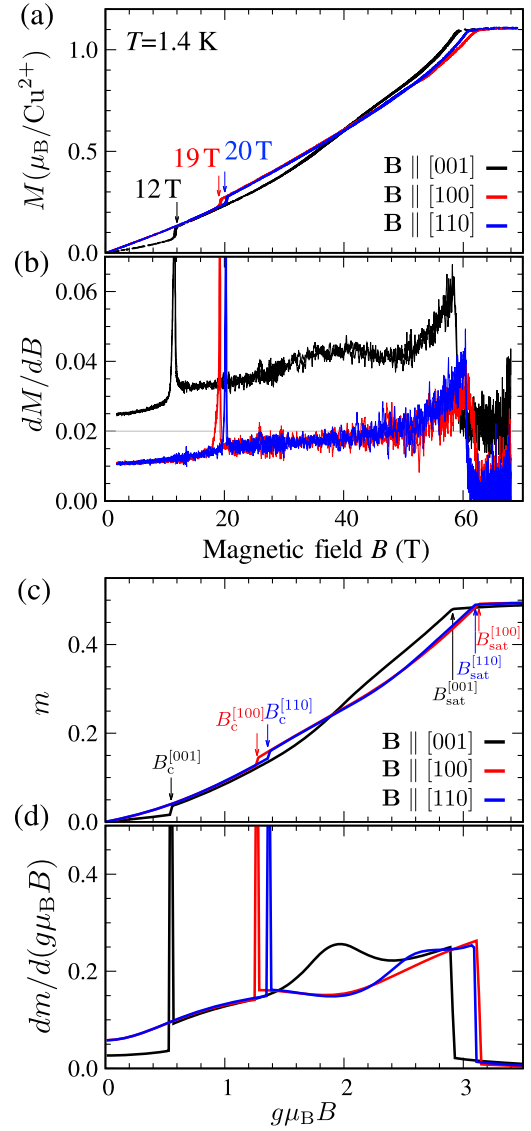

FIG. 2. Magnetic field dependence of magnetization and its field derivative in the (a),(b) experiment for $Ba(TiO)Cu_4(PO_4)_4$ at $T = 1.4$ K (dM/dB for **B**∥[001] is shifted by 0.02 for visibility) and the (c),(d) theory for the model (1) in the ground state with $J_1 = 1$, $J_2 = 1/6$, $J' = 1/2$, $J'' = 1/100$, $\theta = 80°$, and $D = 0.7$.

$$\mathcal{H} = \sum_{\langle i,j \rangle}(J_1 \mathbf{S}_i \cdot \mathbf{S}_j - \mathbf{D}_{ij} \cdot \mathbf{S}_i \times \mathbf{S}_j) + J_2 \sum_{\langle\langle i,j \rangle\rangle} \mathbf{S}_i \cdot \mathbf{S}_j$$
$$+ J' \sum_{(i,j)} \mathbf{S}_i \cdot \mathbf{S}_j + J'' \sum_{[(i,j)]} \mathbf{S}_i \cdot \mathbf{S}_j - g\mu_B \sum_i \mathbf{B} \cdot \mathbf{S}_i, \quad (1)$$

where $\mathbf{S}_i$ represents $S = 1/2$ spin at site i. The sums for $\langle i,j \rangle$, $\langle\langle i,j \rangle\rangle$, (i,j), and $[(i,j)]$ run over J_1, J_2, J', and J'' bonds, respectively. For the intracupola exchange coupling constants, we adopt the estimates from the *ab initio* calculation: $J_1 = 3.0$ meV and $J_2 = 0.5$ meV [7]; we set J_1 as the unit of energy, namely, $J_1 = 1$ and $J_2 = 1/6$. On the other hand, for the intercupola J', we set a larger value, $J' = 1/2$, than the *ab initio* estimate of $J' = 0.7$ meV,

because a small $J' \lesssim 0.4$ leads to a nonmagnetic singlet state in the CMF approach (described below); we set $J'' = 1/100$. The last term in Eq. (1) represents the Zeeman coupling where g and μ_B are the isotropic g factor and the Bohr magneton, respectively.

In the second term in Eq. (1), referring to the Moriya rules [2], we take the DM vector $\mathbf{D}_{ij}$ in the plain perpendicular to the J_1 bond connecting i and j sites with the angle θ_{ij} from the [001] axis [see the yellow arrows in Fig. 1(a)]. Note that the asymmetric buckling of CuO$_4$ plaquettes in the square cupola induces the in-plane component of $\mathbf{D}_{ij}$. The sign of $\mathbf{D}_{ij}$ is reversed between the upward and downward cupolas from the symmetry. We assume uniform $\theta = \theta_{ij}$ and $D \equiv |\mathbf{D}_{ij}|$, and tune the values of θ and D so as to reproduce the magnetization curve in experiments. While the system has the chirality from the alternating twist of square cupolas, ϕ in Fig. 1(b), we omit it for simplicity; the following results remain intact for small ϕ in the real compounds [5].

We calculate the magnetic properties of the model (1) by a standard CMF method, in which the intercupola interactions are treated by the MF approximation. The details are described in the Supplemental Material [8].

Figures 2(c) and 2(d) show the B profiles of magnetization per site m and its field derivative $dm/d(g\mu_B B)$, respectively, obtained by the CMF calculations with $\theta = 80°$ and $D = 0.7$ (we will discuss how to optimize the parameters later). The results reproduce the experimental data well in Figs. 2(a) and 2(b) in the following points. (i) m shows a jumplike anomaly, whose magnetic field depends on the field direction: the anomaly for the out-of-plane field ($\mathbf{B} \| [001]$) appears at $B_c^{[001]}$, which is considerably smaller than $B_c^{[100]}$ and $B_c^{[110]}$ for the in-plane fields $\mathbf{B} \| [100]$ and [110], respectively, and $B_c^{[100]}$ is slightly lower than $B_c^{[110]}$. (ii) The saturation fields, $B_{\mathrm{sat}}^{[100]}$, $B_{\mathrm{sat}}^{[110]}$, and $B_{\mathrm{sat}}^{[001]}$ for $\mathbf{B} \| [100]$, [110], and [001], respectively, satisfy the relationship, $B_{\mathrm{sat}}^{[100]} > B_{\mathrm{sat}}^{[110]} > B_{\mathrm{sat}}^{[001]}$. (iii) $dm/d(g\mu_B B)$ is smaller for $\mathbf{B} \| [001]$ than for $\mathbf{B} \| [100]$ and [110] in the low-field region. (iv) $dm/d(g\mu_B B)$ exhibits a hump at an intermediate field for $\mathbf{B} \| [001]$.

We find that the jumplike anomalies in m originate from the ME phase transitions by elaborating the phase diagram of the model in Eq. (1). Figures 3(a) and 3(c) show the ground-state phase diagrams while varying θ and B for $\mathbf{B} \| [001]$ and [100], respectively, at $D = 0.7$. To identify each phase, we compute the antiferromagnetic order parameter $\mathbf{m}_{\mathrm{AF}}$ and the interlayer-antiferroic electric polarization $\mathbf{P}_{\mathrm{AF}}$, which are defined as $\mathbf{m}_{\mathrm{AF}} = \sum_i (-1)^i p_i \langle \mathbf{S}_i \rangle$ and $\mathbf{P}_{\mathrm{AF}} = \sum_{\langle i,j \rangle} p_i q_i \mathbf{n}_{ij} \langle \mathbf{S}_i \cdot \mathbf{S}_j \rangle$, respectively. The sums run over in the magnetic unit cell shown in Fig. 1(a), $p_i = +1(-1)$ for the upper (lower) layer, and $q_i = +1(-1)$ for the upward (downward) cupolas; $\mathbf{n}_{ij}$ is the normalized vector pointing from the center of the ij bond to the oxygen site shared by the sites i and j. We assume that the electric polarization arises from the exchange striction mechanism [7,9–11]; we confirmed that the inverse DM mechanism [12,13] leads to qualitatively similar behavior [8].

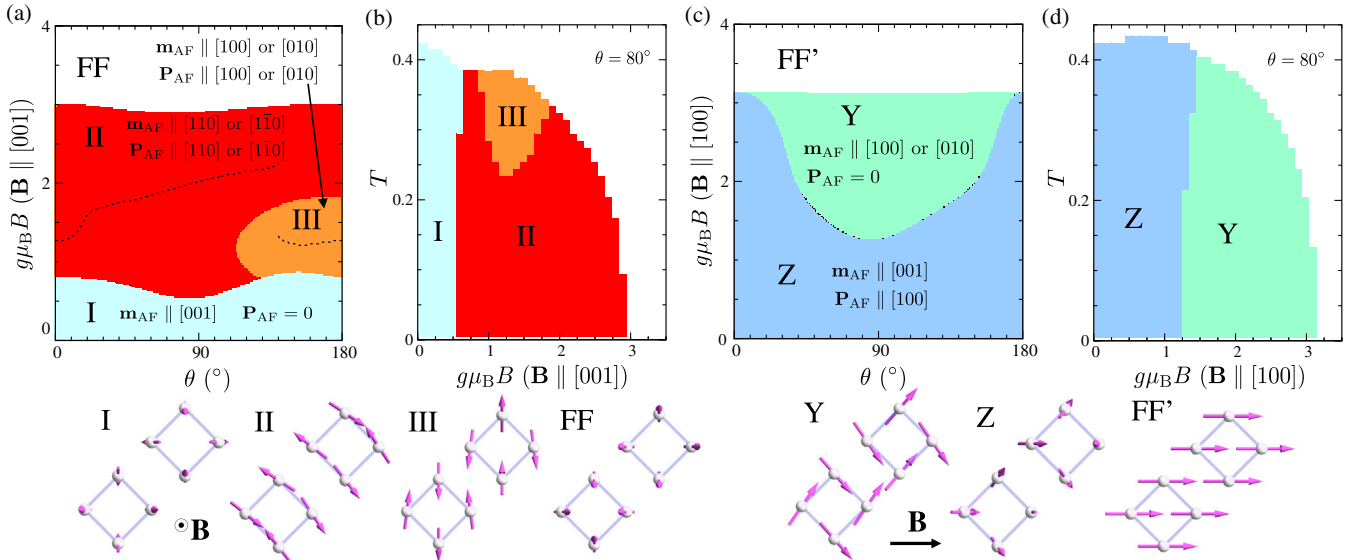At zero field, the ground state of our model exhibits a noncoplanar antiferromagnetic order [8], similar to that

FIG. 3.   Ground-state and finite-T phase diagrams with the magnetic fields (a),(b) $\mathbf{B} \| [001]$ and (c),(d) $\mathbf{B} \| [100]$. In the ground-state phase diagrams (a),(c), the angle θ between $\mathbf{D}_{ij}$ and c axis is varied, and the other parameters are set to be the same as Figs. 2(c) and 2(d). In the finite-T phase diagrams (b),(d), we set $\theta = 80°$ as in Figs. 2(c) and 2(d). The labels I, II, III, Z, and Y identify different antiferromagnetic ordered phases where $\mathbf{m}_{\mathrm{AF}} \neq 0$. FF and FF' are for the forced ferromagnetic phases above the saturation fields. The dashed line in (a) represents the peak position of the hump in dm/dB. Representative spin configurations in each phase are also shown [8].

found in the neutron scattering experiment [7]. For **B**∥[001], we find three phases below the saturation field, as shown in Fig. 3(a). The phases I, II, and III are antiferromagnetically ordered phases; $\mathbf{m}_{AF}\|\mathbf{B}$ and $\mathbf{P}_{AF}=0$ in phase I, while $\mathbf{m}_{AF}\perp\mathbf{B}$ and $\mathbf{P}_{AF}\neq 0$ are in II and III [see also Fig. 4(a)]. Thus, the phases II and III have an interlayer-antiferroic polarization induced by the antiferromagnetic ordering. The magnetization jump appears at the boundary between the paraelectric phase I and the antiferroelectric phase II [$B_c^{[001]}$ in Fig. 2(c)]. We note that the hump appears in dm/dB in phase II, whose position increases as θ [the dashed line in Fig. 3(a)] is increasing. To reproduce this hump, both the quantum fluctuation within the clusters and the in-plane component of $\mathbf{D}_{ij}$ are necessary. For **B**∥[100], on the other hand, we find two antiferromagnetic phases, Z and Y, in both of which $\mathbf{m}_{AF}\perp\mathbf{B}$; $\mathbf{m}_{AF}\|[001]$ and $\mathbf{P}_{AF}\neq 0$ in Z, while $\mathbf{m}_{AF}\|[010]$ and $\mathbf{P}_{AF}=0$ in Y, as shown in Fig. 3(c) [see also Fig. 4(b)]. Also in this case, the magnetization jump appears at the antiferro-paraelectric phase boundary between Z and Y [$B_c^{[100]}$ in Fig. 2(c)]. We note that all of the phase transitions between the different antiferromagnetically ordered phases are of the first order.
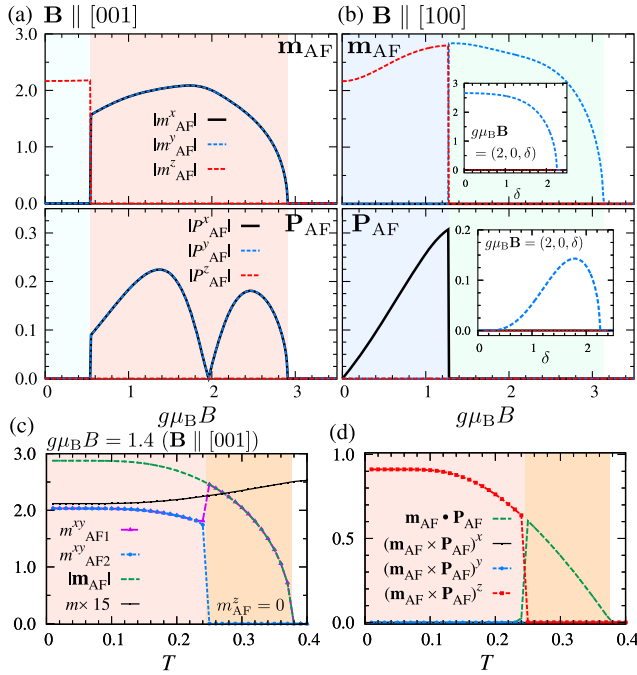

(a) **B** ∥ [001]   (b) **B** ∥ [100]

(c) $g\mu_B B = 1.4$ (**B** ∥ [001])   (d)

FIG. 4. B and T dependence of the antiferromagnetic order parameter $\mathbf{m}_{AF}$ and the interlayer-antiferroic electric polarization $\mathbf{P}_{AF}$ with the parameter set used in Figs. 2(c) and 2(d). The B dependence are computed at $T=0$ for (a) **B**∥[001] and (b) **B**∥[100], while the T dependence of (c),(d) are computed at $B=1.4$ (**B**∥[001]). In addition to $\mathbf{m}_{AF}$, the magnetization m is also plotted in (c); $m_{AF1}^{xy}=\max[m_{AF}^x, m_{AF}^y]$ and $m_{AF2}^{xy}=\min[m_{AF}^x, m_{AF}^y]$. The inner and outer products of $\mathbf{m}_{AF}$ and $\mathbf{P}_{AF}$ are plotted in (d). The insets of (b) show $\mathbf{m}_{AF}$ and $\mathbf{P}_{AF}$ for $\mathbf{B}=(2,0,\delta)$ with varying δ.

Let us comment on how we choose θ and D used above. With regard to D, we find that a sufficiently large $D\sim 0.7$ is necessary to reproduce the experimental value of the ratio $B_c^{[001]}/B_{sat}^{[001]}\sim 1/5$ [8]. A similarly large D has been reported for other Cu-based magnets [14,15]. For θ, we find that $B_c^{[100]}$ takes its minimum at $\theta\simeq 80°$, as shown in Fig. 3(c). Optimizing the values of D and θ to make the ratios $B_c^{[001]}/B_{sat}^{[001]}$ and $B_c^{[100]}/B_{sat}^{[100]}$ closest to the experimental estimates, we obtain $D=0.7$ and $\theta=80°$. We note that the value of θ is in between the weak and strong crystal field limits [8]. The in-plane component of $\mathbf{D}_{ij}$ induced by nonzero θ is crucial to reproduce the experiments.

Figures 3(b) and 3(d) show the finite-T phase diagrams at $\theta=80°$ and $D=0.7$ with **B**∥[100] and [001], respectively. Interestingly, the phase III appears only at finite T and finite B, which evolves from the large θ region at zero T in Fig. 3(a). While m shows a jump at the transition between the phases I and II, a singularity is hardly discernible between II and III [see Fig. 4(c)]. Thus, the phase III is a "hidden" phase in the magnetization measurement. Nonetheless, at the II-III phase boundary, $\mathbf{P}_{AF}$ changes the direction from [110] to [100], and simultaneously, $\mathbf{m}_{AF}$ is switched from $\mathbf{m}_{AF}\perp\mathbf{P}_{AF}$ to $\mathbf{m}_{AF}\|\mathbf{P}_{AF}$ [see Fig. 4(d)]. Thus, the hidden phase III will be identified by the ME measurement in the future [8].

Finally, let us discuss the ME behavior at a finite-T in the low-field region. In the previous experiment, the dielectric constants $\varepsilon_{[100]}$ and $\varepsilon_{[110]}$ show an anomaly at the antiferromagnetic transition in **B**∥[100] and [1$\bar{1}$0], respectively, but not in **B**∥[001]; furthermore, the field-induced components scale with B^2 [7]. Here we compute the dielectric constant as $\varepsilon_{[abc]}=(\langle\mathbf{P}\cdot\mathbf{n}\rangle_{\mathbf{E}=\Delta E\mathbf{n}}-\langle\mathbf{P}\cdot\mathbf{n}\rangle_{\mathbf{E}=0})/\Delta E$, where $\mathbf{n}$ is the normalized vector directing (a, b, c), for the Hamiltonian $\mathcal{H}-\mathbf{E}\cdot\mathbf{P}$; $\mathbf{E}$ is the electric field, and $\mathbf{P}$ is the net polarization defined as $\mathbf{P}\equiv\sum_{\langle i,j\rangle}q_i\mathbf{n}_{ij}(\mathbf{S}_i\cdot\mathbf{S}_j)$, (we set $\Delta E=0.01$). As shown in the inset of Fig. 5, both $\varepsilon_{[100]}$ and $\varepsilon_{[110]}$ show a cusp at the antiferromagnetic transition as observed in the experiments, corresponding to the onset of
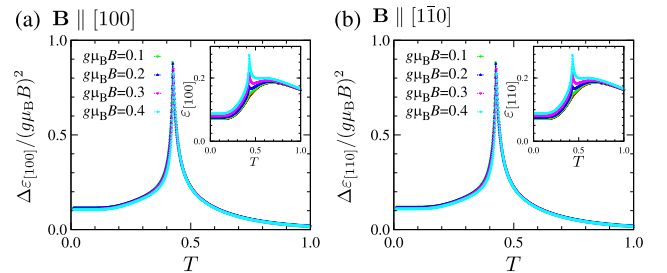

(a) **B** ∥ [100]   (b) **B** ∥ [1$\bar{1}$0]

FIG. 5. The scaling plot for the field-induced component of the dielectric constants: (a) $\Delta\varepsilon_{[100]}$ and (b) $\Delta\varepsilon_{[110]}$ with **B**∥[100] and **B**∥[1$\bar{1}$0], respectively. The insets show (a) $\varepsilon_{[100]}(B)$ and (b) $\varepsilon_{[110]}(B)$.

the antiferroic polarization in the phase Z. Moreover, our results successfully reproduce the scaling behavior $\Delta\varepsilon = \varepsilon(B) - \varepsilon(0) \propto B^2$ for both $\varepsilon_{[100]}$ and $\varepsilon_{[110]}$, as shown in Fig. 5. This scaling is naturally explained by the B-linear behavior of the in-plane polarization [see the lower panel of Fig. 4(b)] and $\varepsilon_{[abc]} \sim \langle (\mathbf{P} \cdot \mathbf{n})^2 \rangle$ expected from the fluctuation-dissipation theorem. We also confirmed not only the absence of dielectric anomalies for $\mathbf{B} \| [001]$ but also a good agreement with the experimental measurements for other orientations of $\mathbf{B}$ and $\mathbf{E}$ [8].

Our exhaustive analysis also predicts a ME response in the phase Y: $\mathbf{P}_{\text{AF}} \| [010]$ is induced by applying $\mathbf{B} \| [001]$ in addition to $\mathbf{B} \| [100]$ [see the insets of Fig. 4(b)]. This is associated with the ME coupling $\propto B^{[001]} E^{[010]}$ in the free energy [8]. We also note that the II–III phase boundary is sensitive to the in-plane component of the electric field: phase III is reduced (extended) by the in-plane field parallel to [110] ([100]). It will be interesting to confirm the ME responses in future experiments.

In summary, we have clarified the ME phase diagram of the antiferromagnets composed of square cupolas by a combined experimental and theoretical study. Our results elucidated how the asymmetric units, made of a small number of spins, activate the ME responses through antisymmetric interactions arising from the spin-orbit coupling. The present study will provide a hint for the design of a new type of ME-active materials originating from such asymmetric units.

[1] I. Dzyaloshinsky, J. Phys. Chem. Solids **4**, 241 (1958).
[2] T. Moriya, Phys. Rev. **120**, 91 (1960).
[3] S.-W. Cheong and M. Mostovoy, Nat. Mater. **6**, 13 (2007).
[4] Y. Tokura, S. Seki, and N. Nagaosa, Rep. Prog. Phys. **77**, 076501 (2014).
[5] K. Kimura, M. Sera, and T. Kimura, Inorg. Chem. **55**, 1002 (2016).
[6] N. A. Spaldin, M. Fiebig, and M. Mostovoy, J. Phys. Condens. Matter **20**, 434203 (2008).
[7] K. Kimura, P. Babkevich, M. Sera, M. Toyoda, K. Yamauchi, G. S. Tucker, J. Martius, T. Fennell, P. Manuel, D. D. Khalyavin *et al.*, Nat. Commun. **7**, 13039 (2016).
[8] See the Supplemental Material at http://link.aps.org/supplemental/10.1103/PhysRevLett.118.107601 for the details of the CMF approximation, the spin configurations in each phase, the electric polarization calculated based on the inverse DM mechanism, the D dependence of the magnetization curves, and the dielectric constants for several orientations of $\mathbf{B}$ and $\mathbf{E}$.
[9] I. A. Sergienko, C. Şen, and E. Dagotto, Phys. Rev. Lett. **97**, 227204 (2006).
[10] S. Picozzi, K. Yamauchi, B. Sanyal, I. A. Sergienko, and E. Dagotto, Phys. Rev. Lett. **99**, 227201 (2007).
[11] K. T. Delaney, M. Mostovoy, and N. A. Spaldin, Phys. Rev. Lett. **102**, 157203 (2009).
[12] H. Katsura, N. Nagaosa, and A. V. Balatsky, Phys. Rev. Lett. **95**, 057205 (2005).
[13] H. J. Xiang, E. J. Kan, Y. Zhang, M.-H. Whangbo, and X. G. Gong, Phys. Rev. Lett. **107**, 157202 (2011).
[14] J. H. Yang, Z. L. Li, X. Z. Lu, M.-H. Whangbo, S.-H. Wei, X. G. Gong, and H. J. Xiang, Phys. Rev. Lett. **109**, 107203 (2012).
[15] J. Sannigrahi, S. Bhowal, S. Giri, S. Majumdar, and I. Dasgupta, Phys. Rev. B **91**, 220407 (2015).